



Heat flow in the rifted continental margin of the South China Sea near Taiwan and its tectonic implications



Wei-Zhi Liao^a, Andrew T. Lin^{a,*}, Char-Shine Liu^b, Jung-Nan Oung^c, Yunshuen Wang^d

^a Department of Earth Sciences, National Central University, No. 300, Jhongda Rd., Jhongli City, Taoyuan County 32001, Taiwan

^b Institute of Oceanography, National Taiwan University, No. 1, Sec. 4, Roosevelt Rd., Taipei 10617, Taiwan

^c CPC Corporation, Taiwan. No. 3, Songren Rd., Sinyi District, Taipei City 110, Taiwan

^d Central Geological Survey, MOEA, No. 2, Lu. 109, Huaxin St., Zhonghe Dist., New Taipei City 235, Taiwan

ARTICLE INFO

Article history:

Received 30 May 2013

Received in revised form 7 December 2013

Accepted 7 January 2014

Available online 17 January 2014

Keywords:

Geothermal gradients

Heat flows

South China Sea

Gas hydrate

ABSTRACT

Temperature measurements carried out on 9 hydrocarbon exploration boreholes together with Bottom Simulating Reflectors (BSRs) from reflection seismic images are used in this study to derive geothermal gradients and heat flows in the northern margin of the South China Sea near Taiwan. The method of Horner plot is applied to obtain true formation temperatures from measured borehole temperatures, which are disturbed by drilling processes. Sub-seafloor depths of BSRs are used to calculate sub-bottom temperatures using theoretical pressure/temperature phase boundary that marks the base of gas hydrate stability zone. Our results show that the geothermal gradients and heat flows in the study area range from 28 to 128 °C/km and 40 to 159 mW/m², respectively. There is a marked difference in geothermal gradients and heat flow beneath the shelf and slope regions. It is cooler beneath the shelf with an average geothermal gradient of 34.5 °C/km, and 62.7 mW/m² heat flow. The continental slope shows a higher average geothermal gradient of 56.4 °C/km, and 70.9 mW/m² heat flow. Lower heat flow on the shelf is most likely caused by thicker sediments that have accumulated there compared to the sediment thickness beneath the slope. In addition, the continental crust is highly extended beneath the continental slope, yielding higher heat flow in this region. A half graben exists beneath the continental slope with a north-dipping graben-bounding fault. A high heat-flow anomaly coincides at the location of this graben-bounding fault at the Jiulong Ridge, indicating vigorous vertical fluid convection which may take place along this fault.

© 2014 Elsevier Ltd. All rights reserved.

1. Introduction

The South China Sea rifted margin is characterized by highly attenuated continental crust and in typical rifted continental margins, heat flow may range from 40 to 70 mW/m² in average (Allen and Allen, 2005). The magnitude of heat flow and its distribution are combined effects of tectonic development and sedimentation in the continental margin (e.g., Cloetingh et al., 2010). A study of the spatial heat-flow distribution in a rifted margin may therefore reveal important tectonic features and shed lights on the tectonic development of the studied margin. The northern continental margin of the South China Sea (SCS) is occupied by rift basins that extend from beneath the continental shelf to continental slope. From east to west, the rift basins are the Tainan Basin (Yang et al., 1991; Lee et al., 1993; Tzeng et al., 1996), Pearl River Mouth Basin (Watson et al., 1987; Wu, 1988; Yu, 1990, 1994), and Qiongdongnan Basin (Wu, 1988). The study area lies in the

northeastern corner of the SCS continental margin where the rifted continental margin (i.e. the Tainan Basin) has been overridden by the Taiwan orogenic wedge in the east since the late Miocene (Lin and Watts, 2002; Lin et al., 2003, 2008). The oblique impingement of the orogenic wedge on top of the rifted continental margin has turned the rifted continental margin into a mature foreland basin in the north (Lin and Watts, 2002) and an incipient foreland basin in the south, especially in the continental slope (Yu and Hong, 2006). The superposition of foreland basin on top of the rifted continental margin may result in a significant change of heat-flow patterns from typical rifted continental margins.

The western part of the northern continental margin (i.e. the Pearl River Mouth Basin and the Qiongdongnan Basin) of the SCS is a region of high heat flow compared to other rifted continental margins; with heat flow ranging from 50 to 120 mW/m² (Yuan et al., 2009). There is a general trend that heat flow increases from the inner margin to the outer margin (Shi et al., 2003). One reason for the high heat flow in this margin is that it is geologically young, merely 32 Ma old (Taylor and Hayes, 1983; Briaes et al., 1993). Another reason may be vigorous magmatic activities associated

* Corresponding author. Tel.: +886 3 4227151x65618; fax: +886 3 4222044.

E-mail address: andrewl@ncu.edu.tw (A.T. Lin).

with rifting processes occurring especially in the outer margin (Yuan et al., 2009). In addition, recent episodes of Miocene and Pliocene crustal extensions (He et al., 2001; Clift and Lin, 2001) may also assist to raise the heat flows in this margin.

The heat flow pattern in the eastern part of northern continental margin near Taiwan (i.e. the Tainan Basin) is unclear due to a lack of study. While the heat flows in the submarine accretionary wedge has been reported in the literature (Chi et al., 2003; Chi and Reed, 2008; Shyu et al., 2006) using the lower phase boundary of the gas hydrate stability zone inferred from seismic sections as Bottom Simulating Reflectors (BSRs). Past studies show that the average heat flow ranges from around 64 mW/m^2 (Shyu et al., 2006) to 43 mW/m^2 (Chi and Reed, 2008) in the submarine accretionary wedge neighboring the rifted continental margin.

The studied continental margin (i.e. the Tainan basin) lies in the junction area between the rifted continental margin in the west and the accretionary wedge in the east. In terms of tectonic development, this area evolved from a rifted margin to a foreland basin. In this study, we first establish thermal gradients using data of

bottom hole temperatures, measurements from hydrocarbon exploration wells in the shelf region and BSRs beneath the continental slope. These thermal gradients are then converted to heat flows with inferred thermal conductivities for studied sediment sections. The spatial distribution of heat flow allows us to gain a better understanding of the thermal regime in this tectonic transition zone.

2. Regional geological setting

The Tainan Basin is a Paleogene rift basin in the northeastern margin of the South China Sea, consisting of three tectonic elements, namely, the Northern Depression, Central Uplift Zone, and Southern Depression (Fig. 1; Tsao et al., 1992; Lin et al., 2003). The Northern Depression and Central Uplift Zone lie beneath the shelf region (Yang et al., 1991; Lee et al., 1993; Tzeng et al., 1996; Tang et al., 1999; Lin et al., 2003) while the Southern Depression lies largely beneath the continental slope (Fig. 1). A series of ENE-trending normal faults developed beneath the shelf

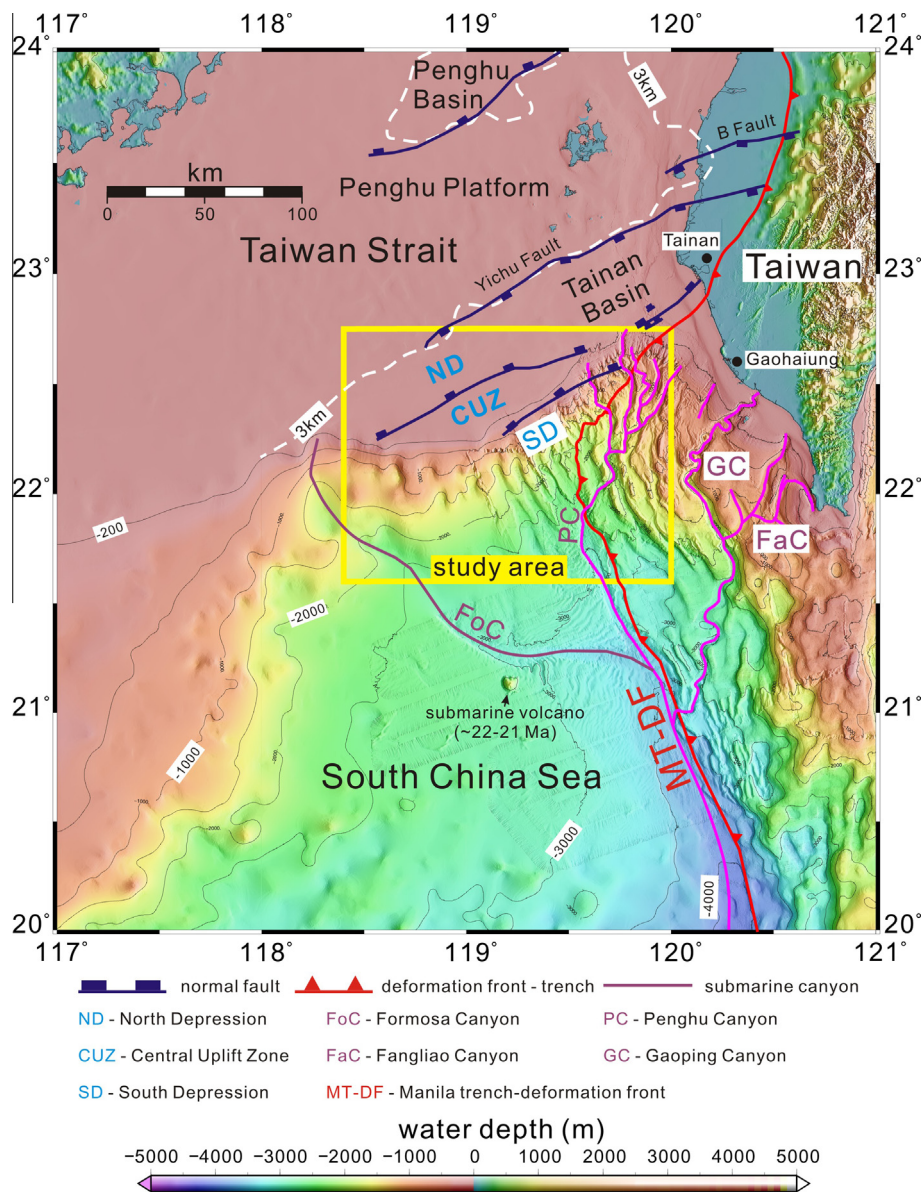


Fig. 1. Bathymetry and tectonic features off southwest Taiwan. Tectonic elements and sediment isopach of 3000 m are from Lin et al. (2003). The age of a submarine volcano south of the Formosa Canyon is from Wang et al. (2012) Purple lines reveal the course of submarine canyons. The yellow rectangle marks the study area.

(Yang et al., 1991) with one major north-dipping, graben-bounding fault lying beneath the upper continental slope in the west (Li et al., 2007; Yeh et al., 2012; Lester et al., 2012). Li et al. (2007) and Lester et al. (2012) assume that this fault is the northern boundary of the Central Uplift Zone. Another important fault in the study area is a south-dipping active fault in the outer shelf and near the shelf break east of Tainan Basin (Lin et al., 2008, Fig. 2). High relief (~50 m) of the fault scarp at the seafloor, rotated hangingwall strata, and stratal truncation beneath the upper slope indicate that this emergent fault is a major and active growth normal fault (Lin et al., 2003, 2008). According to the existence of this fault, Lin et al. (2008) divided the slope region into an eastern and a western region with the fault pertaining to the eastern segment.

The continental slope offshore southern Taiwan is named “Tainan Continental Slope”, for simplicity, in this study. A series of NNW-SSE trending bathymetric ridges and erosional gullies characterize the bathymetry of the slope (Fig. 2; Liu et al., 1998, 2004). Bottom simulating reflectors exist especially beneath the ridges, indicating the presence of gas hydrates beneath those bathymetric highs (Liu et al., 2006; Lin et al., 2009). Significant patches of authigenic carbonates are found in water depths ranging from 500 to 800 m on the westernmost bathymetric ridge of the Tainan Continental Slope. This ridge is named as Jiulong Methane Reef by Suess (2005) and Han et al. (2005). The term “reef” is designated to describe the existence of authigenic carbonates though those carbonates are not of coral reef origin. Considering that, reef is not a proper term to describe a submarine bathymetric feature, we name this authigenic carbonate-bearing ridge “Jiulong Ridge” in this study (Fig. 2). The ridge potentially hosts a large

amount of gas hydrate (e.g., Li et al., 2013). Along the Tainan Continental Slope, the Formosa Ridge (Fig. 2) is another important ridge with gas-hydrate bearing signatures, such as continuous BSRs and seafloor gas vents (Liu et al., 2006; Chiu et al., 2006; Lin et al., 2009).

3. Data and methods

Heat flow may be considered the products of geothermal gradient at a particular depth interval and the thermal conductivity for sediment section where the geothermal gradient is measured. Two types of data are available for us to determine the geothermal gradients in the study area. There are 9 hydrocarbon exploration wells in the shelf available for this study (Table 1 and Fig. 2). Beneath the

Table 1
Table showing basic information for boreholes used in this study.

Borehole	Water depth (m)	Drill depth (m)	Formation age at drill depths
A-1	93	2640	Lower cretaceous
C-4	127	3912	Lower cretaceous
C-5	130	3754	Lower cretaceous
C-6	110	4100	Lower cretaceous
C-7	135	3896	Lower cretaceous
F-1	128	3947	Lower cretaceous
J-1	86.9	4850	Oligocene
A-1J	142	3653	Lower cretaceous
F-1D	149	3848	Lower cretaceous

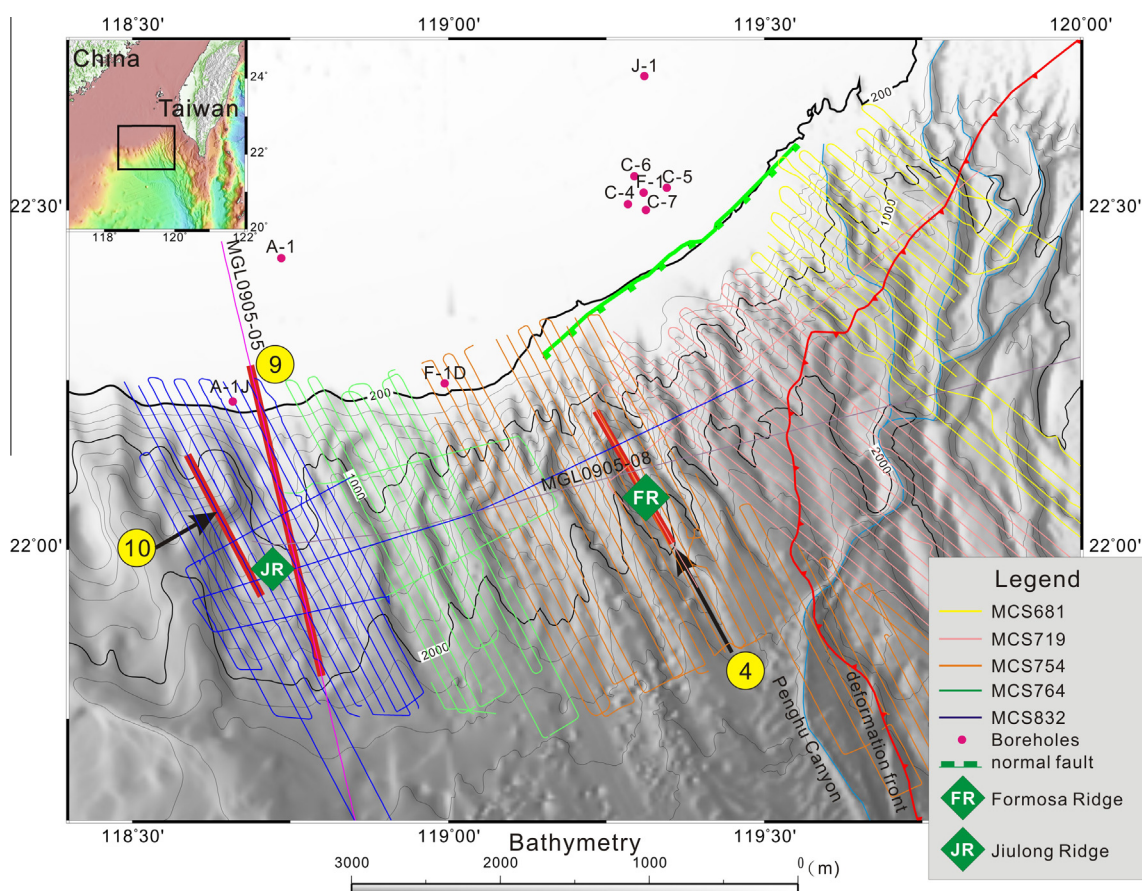


Fig. 2. Bathymetric features and data distribution in the study area. An emergent normal fault is marked in light green line (Lin et al., 2008). It exists near the shelf break at the eastern part of continental margin. Red dots on the shelf indicate the locations of boreholes used in this study. Colored lines in the slope region show different sets of reflection seismic data used in this study. Thick red lines are seismic sections shown in their respective figures with figure numbers shown in the yellow circles.

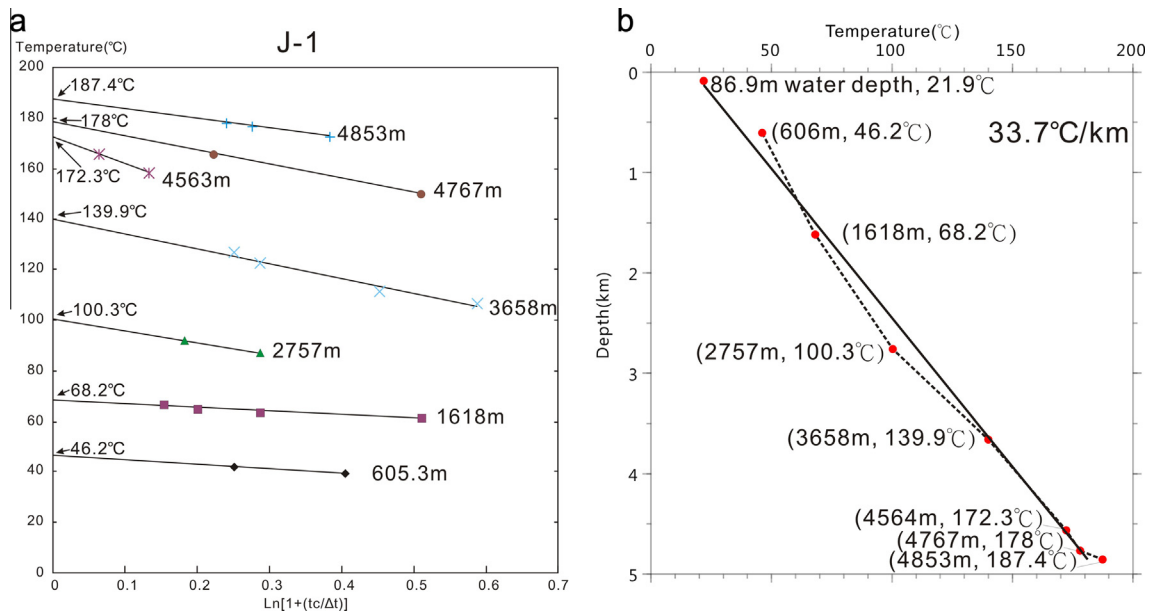


Fig. 3. An example from J-1 well showing (a) Horner-Plot method for obtaining virgin rock temperatures (or corrected temperatures) at successive measured depths, and (b) corrected temperatures at measured depths (red dots) and best-fit trend line of the geothermal gradient for the borehole. In (a), two or more measured temperatures (BHTs) in each depth are used to obtain corrected temperatures. The interceptions of the trend lines for each depth indicate corrected temperatures shown alongside an arrow. In (b), the dashed line connecting each corrected temperature to shows the general trend of geothermal gradient at this borehole. A solid line is the best-fit trend line of the borehole temperatures to represent the geothermal gradient at this borehole, the value (33.7 °C/km) is shown at the upper-right corner of this figure and is used to calculate the heat flows in the shelf area. See texts for details. (For interpretation of the references to color in this figure legend, the reader is referred to the web version of this article.)

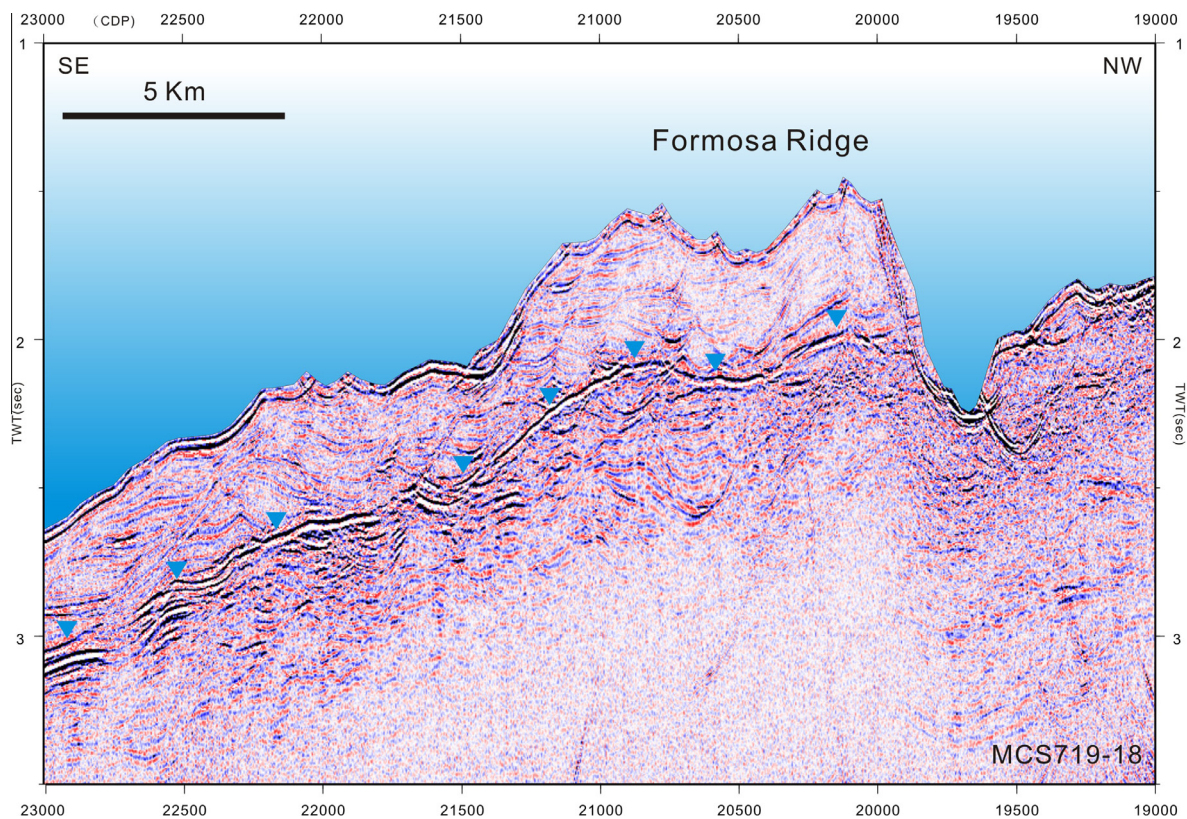


Fig. 4. An example seismic section along the Formosa Ridge shows a clear BSR running beneath the continual slope. Inverted blue triangles indicate the location of the BSR. Characteristic features of BSRs are as follows: the BSR is almost parallel to the seafloor showing reversed polarity of the seafloor reflectors, and strong reflections beneath BSRs. The location of this seismic profile is shown in Fig. 2. (For interpretation of the references to color in this figure legend, the reader is referred to the web version of this article.)

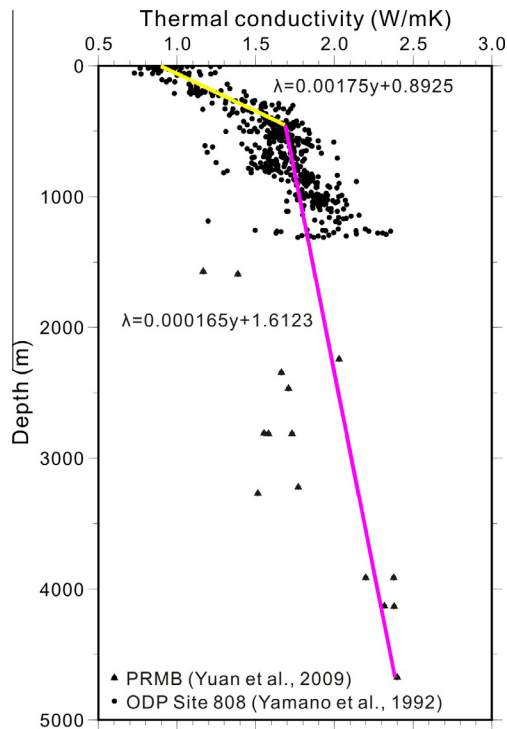


Fig. 5. Variations of thermal conductivity with increasing depths compiled from data as reported in Yamano et al. (1992) (0–1400 m sub-seafloor depths from ODP Site 808) and Yuan et al. (2009) (1500–4600 m from hydrocarbon exploration wells in Pearl River Mouth Basin). Averaged values of thermal conductivity are approximated by two fitted lines above and below 450 m depth, respectively. Averaged values of thermal conductivity are used to calculate heat flow in the shelf region.

continental slope, we use BSR sub-bottom depths from a dense grid of multichannel reflection seismic (MCS) data to constrain geothermal gradients in the slope.

For bottom hole temperatures measured in boreholes, the measured temperature is disturbed by drilling processes (e.g. mud circulation), and it therefore does not represent the true formation temperature (Beardmore and Cull, 2001). A correction must be applied to obtain true formation temperatures. We follow the common practice used in the oil industry (i.e., Horner-plot method) to obtain true formation temperatures from measured temperatures (Horner, 1951; Lachenbruch and Brewer, 1959; Walpes and Ramly, 2001; Waples and Pedersen, 2004). The equation for this method states that

$$\text{BHT} = \text{VRT} + \left(\frac{H}{4\pi\lambda} \right) \times \text{Ln} \left[1 + \left(\frac{t_c}{\Delta t} \right) \right] \quad (1)$$

where BHT means bottom-hole temperature and VRT indicates virgin rock temperature, t_c is the time elapsed between cessation of drilling and cessation of fluid circulation, Δt is the time elapsed between cessation of fluid circulation and measurements of BHT, λ is the thermal conductivity of the rock, and H is the rate of heat supplied to the well. VRT will be the same as BHT while $\text{Ln}[1 + (t_c/\Delta t)]$ equals zero. An example plot of temperature versus $\text{Ln}[1 + (t_c/\Delta t)]$ is shown in Fig. 3a. Using this method, VRTs (or corrected temperatures) of different measured sub-bottom depths can be found for each borehole.

The Horner-plot method needs at least two data sets (i.e. two temperature values measured at different times) at a particular depth in order to fit a trend line and obtain the true formation temperature. Fig. 3a shows an example using Horner-plot method for borehole J-1 in this study. A similar correction is applied to each

Table 2

Table showing corrected temperatures at measured depths (referenced to Kelly bushing on the drilling platform), thermal gradients, and heat flow values from studied boreholes. See texts for details of each parameter. The heat flow values are the products of thermal conductivity and the interval thermal gradients marked as bold letters.

Borehole (water depth, seafloor temperature)	Measured depth (m)	Corrected temperature (°C)	Thermal gradient (°C/km)		Thermal conductivity (W/mK)	Heat flow value (mW/m ²)
			Averaged thermal gradients	Interval Thermal gradients		
A-1 (93 m, 21.4 °C)	406	40.6	24.9	–	1.58	39.28
	1520	68.3		32.9		
C-4 (127 m, 19 °C)	1796	66.9	41.9	–	1.84	76.98
	1956	67.9		26.8		
	3236	126.2		34.5		
	3699	137.5		33.2		
	3913	157.6		36.6		
C-5 (130 m, 18.8 °C)	623	35.0	37.4	–	1.82	68.15
	1815	76.2		34.1		
	3099	125.2		35.8		
	3756	152.3		36.8		
C-6 (110 m, 20.1 °C)	611	38.9	34.8	–	1.84	64.28
	2015	75.7		29.2		
	3214	124.9		33.8		
	4104	159.2		34.8		
C-7 (135 m, 18.5 °C)	621	43.3	37.6	–	1.82	68.61
	1775	67.7		30.0		
	3351	135.2		36.3		
	3764	160.9		39.2		
F-1 (128 m, 18.9 °C)	499	33.9	38.0	–	1.84	64.64
	1569	65.5		32.4		
	2300	97.2		36.1		
	3022	133.9		40.0		
	3376	135.7		36.0		
	3523	146.0		37.5		
	3951	142.5		32.3		

(continued on next page)

Table 2 (continued)

Borehole (water depth, seafloor temperature)	Measured depth (m)	Corrected temperature (°C)	Thermal gradient (°C/km)		Thermal conductivity (W/mK)	Heat flow value (mW/m ²)
			Averaged thermal gradients	Interval Thermal gradients		
J-1 (86.9 m, 21.9 °C)	605	46.2	33.7	–	1.92	64.61
	1618	68.2		30.2		
	2757	100.3		29.4		
	3658	139.9		33.0		
	4564	172.3		33.6		
	4767	178.1		33.4		
	4853	187.4		34.7		
A-1J (142 m, 18.1 °C)	621	38.0	24.7	–	1.78	43.86
	1716	70.0		33.0		
	3267	103.8		27.4		
F-1D (149 m, 17.7 °C)	1758	64.1	40.3	–	1.83	73.87
	3166	116.3		32.7		
	3847	149.6		35.7		

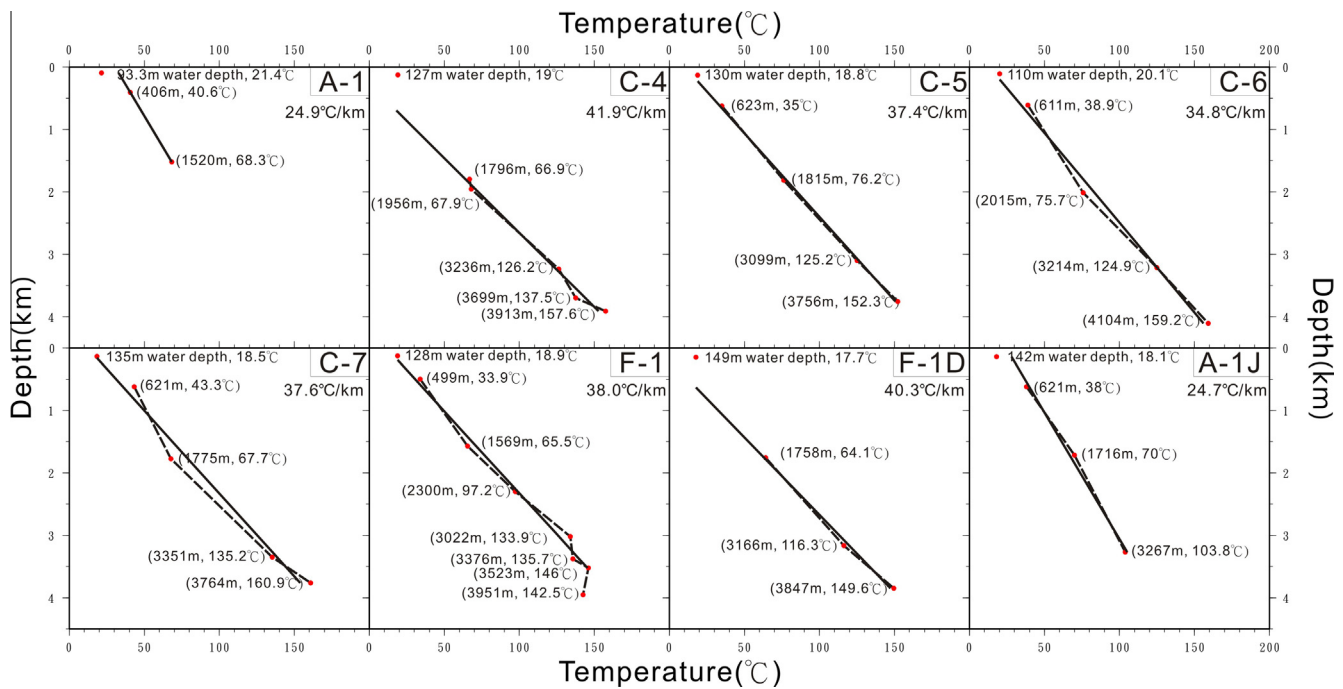


Fig. 6. Corrected temperature vs. depth plots for the studied boreholes in the shelf region (see Fig. 2 for borehole locations). The dashed black lines connect corrected temperatures at each measured depth (red dots) and the solid lines show the best-fit line for geothermal gradient at each borehole with values shown at the lower left corner at each figures. The value of geothermal gradient in the upper right corner of each figure indicates the geothermal gradient used to calculate heat flows in this study.

measured depth with multiple temperature measurements. The VRT at successive depths, and therefore the geothermal gradient in the borehole, can be found as shown in Fig. 3b.

In the continental slope, the geothermal gradient is determined by estimated temperatures at the water/seafloor interface and at the BSRs seen from seismic sections. The BSR represents the lower boundary of the gas hydrate stability zone and it is determined by pressure and temperature conditions (Stoll et al., 1971; Hyndman et al., 1992). Fig. 4 shows an example seismic section running perpendicular to the strike of the continental slope and parallel to the Formosa Ridge, featuring a characteristic BSR on the continental slope. Once the sub-bottom depths and hence pressures at the depth of BSR are known, true formation temperatures can be calculated. The pressure at the BSR sub-bottom depth is calculated by the following formula,

$$P = \rho_w gZ + \rho g y + P_0 \quad (2)$$

where ρ_w is the density of water, ρ is the sediment density above BSR, Z is water depth, y is BSR sub-bottom depth, and P_0 is atmospheric pressure. The temperature T at BSR is derived from the formula (Gayet et al., 2005; Liu et al., 2006)

$$\begin{aligned} \ln(P/P_0) &= 33.4 - 8245/T, & 275.15 \text{ K} \leq T \leq 286.15 \text{ K} \\ \ln(P/P_0) &= 41.636 - 10602/T, & 286.15 \text{ K} \leq T \leq 300.15 \text{ K} \end{aligned} \quad (3)$$

Temperature at water/seafloor interface is calculated by the following equation derived from measured water temperature (Chi and Reed, 2008) from database collected by National Center of Ocean Research of Taiwan,

$$T_{SF} = 0.2597 \times (\ln Z)^3 - 3.802 \times (\ln Z)^2 + 10.67 \times (\ln Z) + 26.96 \quad (4)$$

where T_{SF} is the temperature of seafloor in °C, $\ln Z$ is the natural log of water depth in meter. Once the seafloor temperatures and temperatures at BSR sub-bottom depths are known, geothermal

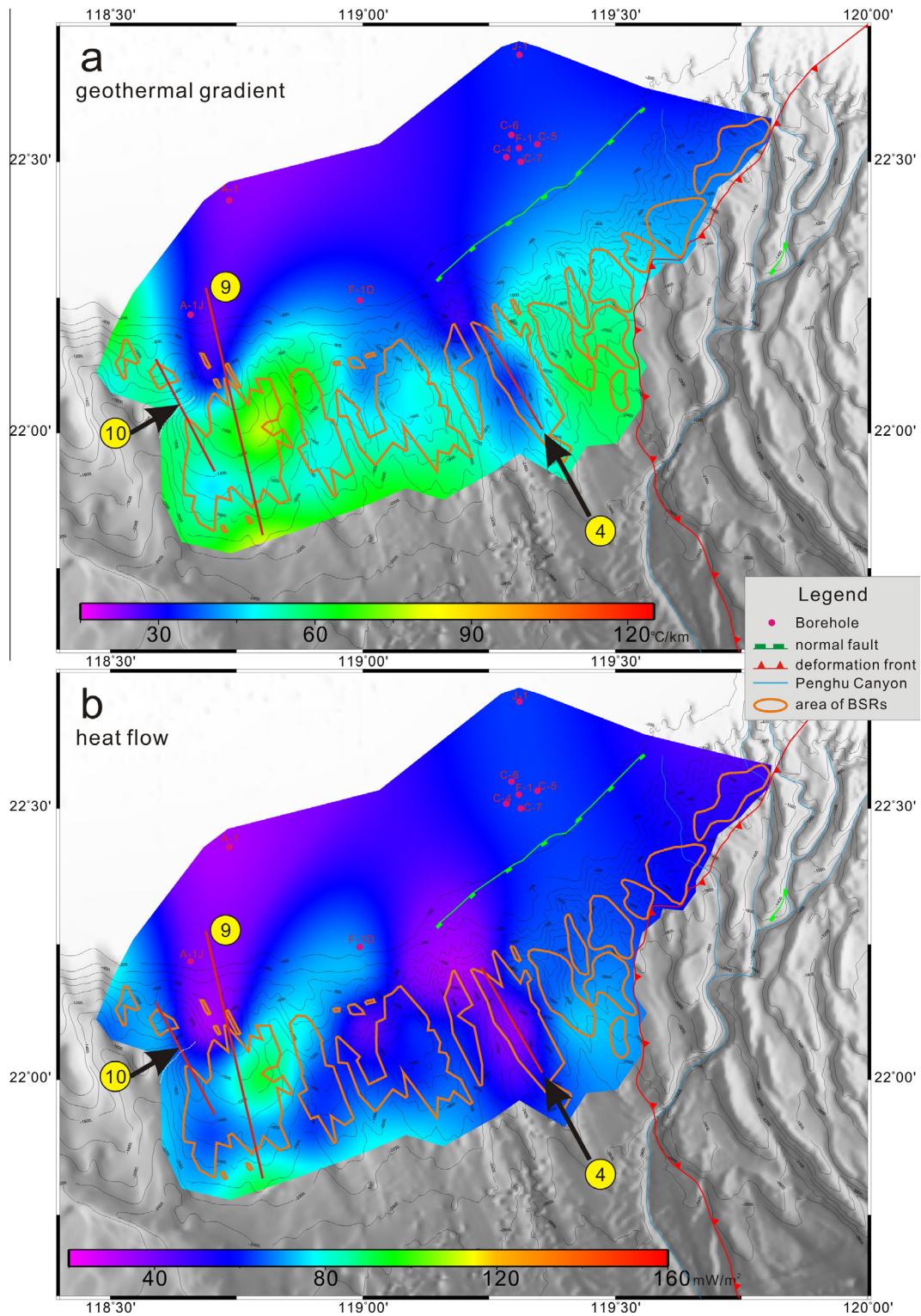


Fig. 7. Bathymetric maps off SW Taiwan with superimposed distribution of geothermal gradient (a) and heat flows (b).

gradients in the continental slope can be obtained. Sediment thermal conductivity is another important parameter for calculating heat flows in a particular area. Thermal conductivity of sediments is governed by mineral compositions, amount of porosity, and type of pore fluid (Beardsmore and Cull, 2001). As there is no direct measurement of sediment thermal conductivity available for this study, an indirect method for determining sediment conductivities must be applied. According to Houbolt and Wells (1980), sediment

thermal conductivity is a function of sediment P -wave velocity, V (km/s), and temperature, T (°C), of the following form

$$\lambda = 77 \times V / [a \times (c + T)] \quad (\text{Wm}^{-1}\text{°C}^{-1}), a = 1.039, \text{ and } c = 80.031. \quad (5)$$

For the slope region, Shyu et al. (2006) measured thermal conductivity for seafloor sediments in this region. Sediment thermal conductivity at BSR depth can be estimated from velocity and

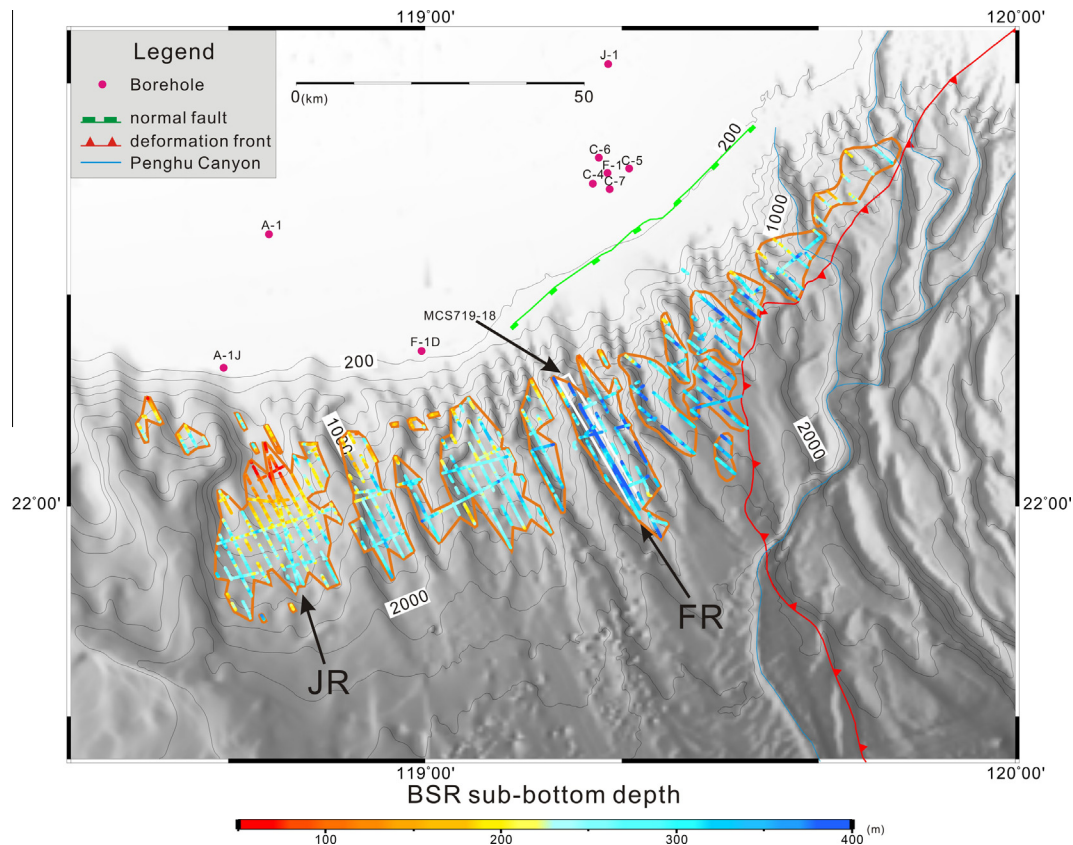


Fig. 8. Bathymetric map of the study area showing distribution and depths of BSRs in the Tainan continental slope. Depths of BSRs are shown in red to blue colors with increasing depths. The enclosed and brown solid lines indicate regions with abundant BSR distribution. Red dots in the continental shelf are hydrocarbon exploration boreholes with temperature measurements available for this study. The white line running along the Formosa Ridge (FR) shows the location for seismic profile MCS719-18, which is shown in Fig. 4.

temperature at BSR. The sediment velocity at BSR depth was given by Lin et al. (2013) and sediment temperature at BSR depth can be derived from Eq. (3). Once the above parameters are known, sediment thermal conductivity at BSR depths can be obtained using Eq. (5). The averaged sediment thermal conductivities (λ_{av}) above BSR can be obtained by the following formula (Beardsmore and Cull, 2001)

$$\lambda_{av} = \frac{y}{(y_1/\lambda_1 + y_2/\lambda_2 + y_3/\lambda_3 + \dots)} \quad (6)$$

where y is total thickness of the layer (equals to BSR sub-bottom depth in this case and total drill depth if it is a borehole). Each paired y and λ (y_1 and λ_1 , y_2 and λ_2 , etc.) are the thickness and thermal conductivity of each measured (or derived) layer. In this study, we only have two pairs of y and λ (upper layer and lower layer) to calculate thermal conductivities in the slope region.

Thermal conductivities converted by Eq. (5) are reasonable for shallow layer (<1000 m). However, unreasonable and low thermal conductivity values are found in deeper depths (i.e., >1000 m). To rectify this problem, we use thermal-conductivity measurements on core samples to obtain more realistic thermal conductivity for sediments deeper than 1000 m. Mudstone is the main lithology for Tainan Basin (Lin et al., 2003) we therefore compile thermal conductivity measurements from mudstones from different sources to infer thermal conductivities for the studied sediment sections. Yamano et al. (1992) reported thermal conductivities measured from ODP Site 808 for the uppermost 1400 m of mudstone, whereas Yuan et al. (2009) reported mudstone thermal conductivities from the neighboring Pearl River Mouth Basin for deeper depths ranging from ~1500–4600 m. Fig. 5 shows a plot for variations of thermal

conductivity with increasing depths compiled from the above two reports. The thermal conductivity versus depth relationship is approximated by a straight line of the form, $\lambda = 0.00175y + 0.8925$, for sub-bottom depth shallower than 450 m; and $\lambda = 0.000165y + 1.6123$ for sub-bottom depth deeper than 450 m, where λ is thermal conductivity in W/m °C, and y is depth in meter beneath seafloor. Thermal conductivities for hydrocarbon exploration wells in the shelf region are obtained by using Eq. (6) with 10 m as increment (e.g., 0–10, 10–20...) and values of thermal conductivity given by above two fitted trend lines. The averaged thermal conductivities for each borehole are shown in Table 2.

4. Results

4.1. Geothermal gradients and heat flows from boreholes in the shelf region

Table 2 listed the results of corrected temperatures (i.e. Virgin Rock Temperature, VRT) at measured depths, geothermal gradients, shallow sediment thermal conductivities and heat flows. Figs. 3 and 6 show corrected temperatures with increasing depths and calculated thermal gradients for boreholes used in this study. Thermal gradients are given as two forms: (1) values obtained from the temperature difference between each measured depth (i.e., interval thermal gradients shown in Table 2), (2) averaged thermal gradients for the total depths of each borehole fitted by using the least square method. The fitted line can be visualized in Figs. 3 and 6. The values of averaged thermal gradients are listed in Table 2 and shown at the top right corner for each temperature vs. depth plot of boreholes as shown in Figs. 3 and 6. From the figures one

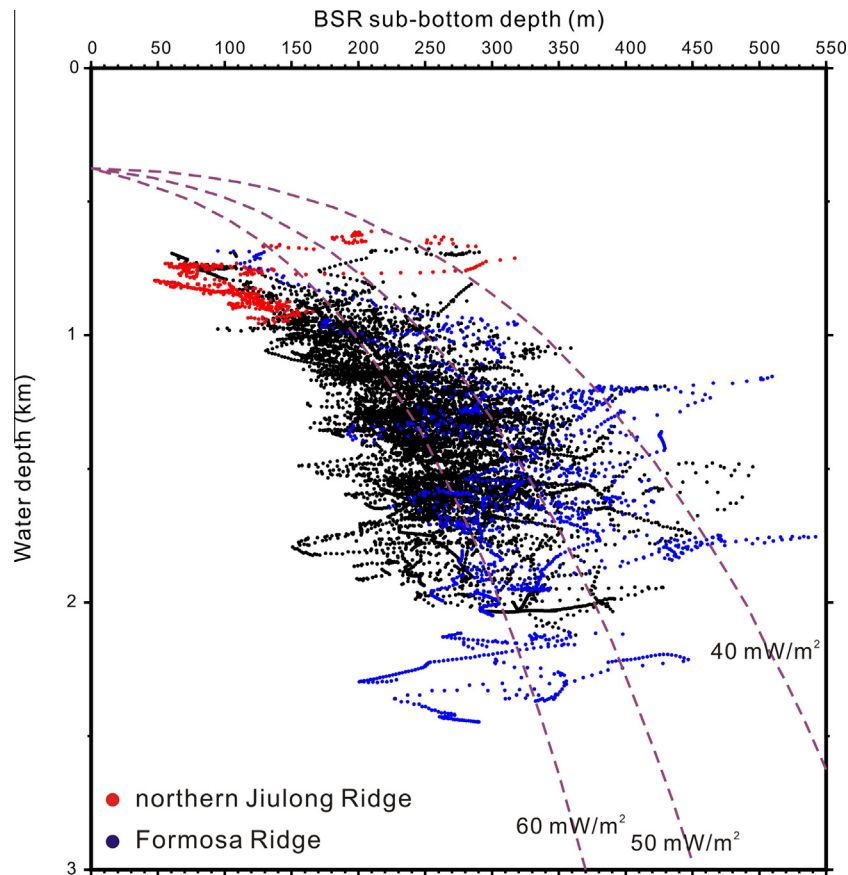


Fig. 9. Cross plots of water depths and BSR sub-bottom depths in the slope region. Dashed curves are the calculated gas hydrate stability curves for different heat flow values (assuming average temperature on the seafloor = 2.850 °C and average thermal conductivity of the sediments = 1.00 W/mK, Shyu et al., 2006).

finds that the linear thermal gradient fits the observed data well, with thermal gradients ranging from 24.7 °C/km (A-1J well) to 41.9 °C/km (C-4 well). There are some deviations of the corrected temperatures from the linear trend lines, especially in deeper depths, due perhaps to anomalous fluid flows in hydrocarbon reservoirs (e.g., the interval between 3022 m and the drilled total depth at the F-1 well).

Heat flows in the shelf region is derived from the product of thermal gradient (marked as bold texts in Table 2) and thermal conductivity as mentioned in Section 3. Calculated heat flows range from around 39–77 mW/m² in the shelf (Table 2 and Fig. 7b).

4.2. Geothermal gradients and heat flows from BSRs in the slope region

BSRs are ubiquitous in the Tainan continental slope beneath water depths ranging from 600 m to around 2500 m (this study and Lin et al., 2009, Fig. 8). The spatial distribution of BSRs shows that, in the western part of the slope, BSRs cluster especially beneath the ridges but are absent in gullies. In the eastern slope, BSRs prevail both beneath gullies and ridges. We use a sediment velocity function obtained from sonic logs as reported in Lin et al. (2013) to convert BSR travel times into sub-bottom depths. Results show that BSR sub-bottom depths range mostly from 150 m to 350 m with a few excursions (Figs. 8 and 9). An area with anomalously deep BSR sub-bottom depths, up to 400 m, is observed to lie beneath the Formosa Ridge. Another area with anomalously shallow BSR sub-bottom depths, ranging from 50 to 150 m, is found in the Jiulong Ridge at a water depth of 700 m to 1000 m (Figs. 8 and 9).

The seafloor temperature ranges from 2 to 17 °C in the slope assuming that the temperature on the seafloor/sediment interface is similar to that of the seawater. The derived temperature at BSR

mostly spans from 21 to 11 °C. With known temperatures both at seafloor and BSR, the geothermal gradients in the slope region can then be readily derived. Fig. 7a shows the spatial distribution of geothermal gradients both in the shelf and slope regions for the Tainan Basin. The geothermal gradient in the slope region spans a wide spectrum, varying from 28 to 128 °C/km with an averaged geothermal gradient of 56.4 °C/km. An anomalous area with higher geothermal gradients (greater than 100 °C/km) is found at the northern part of the Jiulong Ridge (Fig. 7a). By contrast, an anomalous area with lower geothermal gradients (less than 30 °C/km) is found at the Formosa Ridge (Fig. 7a).

The heat flow map (Fig. 7b) shows that heat flow ranges between 50 and 100 mW/m², with an average of 70.9 mW/m² in the slope region. A high heat flow anomaly, of up to 159 mW/m², is found at the Jiulong Ridge in the slope. A low heat flow anomaly is discovered on the Formosa Ridge with lowest heat flow values around 40 mW/m².

5. Discussion

The spatial distribution of geothermal gradients and heat flows (Fig. 7) indicates that geothermal gradients and heat flows are lower in the continental shelf and higher in the slope region. We argue that thick Cenozoic sediment covers (Lin et al., 2003) and rapid sedimentation rate (Tzeng et al., 1996) are main governing factors for relatively low geothermal gradients and heat flow in the continental shelf. The Cenozoic sediments in the Tainan Basin are about 4 km to 10 km thick (Lin et al., 2003) and average sedimentation rate is around 600 m/Myrs since the Pliocene in the shelf region (Tzeng et al., 1996). These features possibly prohibit efficient heat transfer from basement to the shallow subsurface and hence result

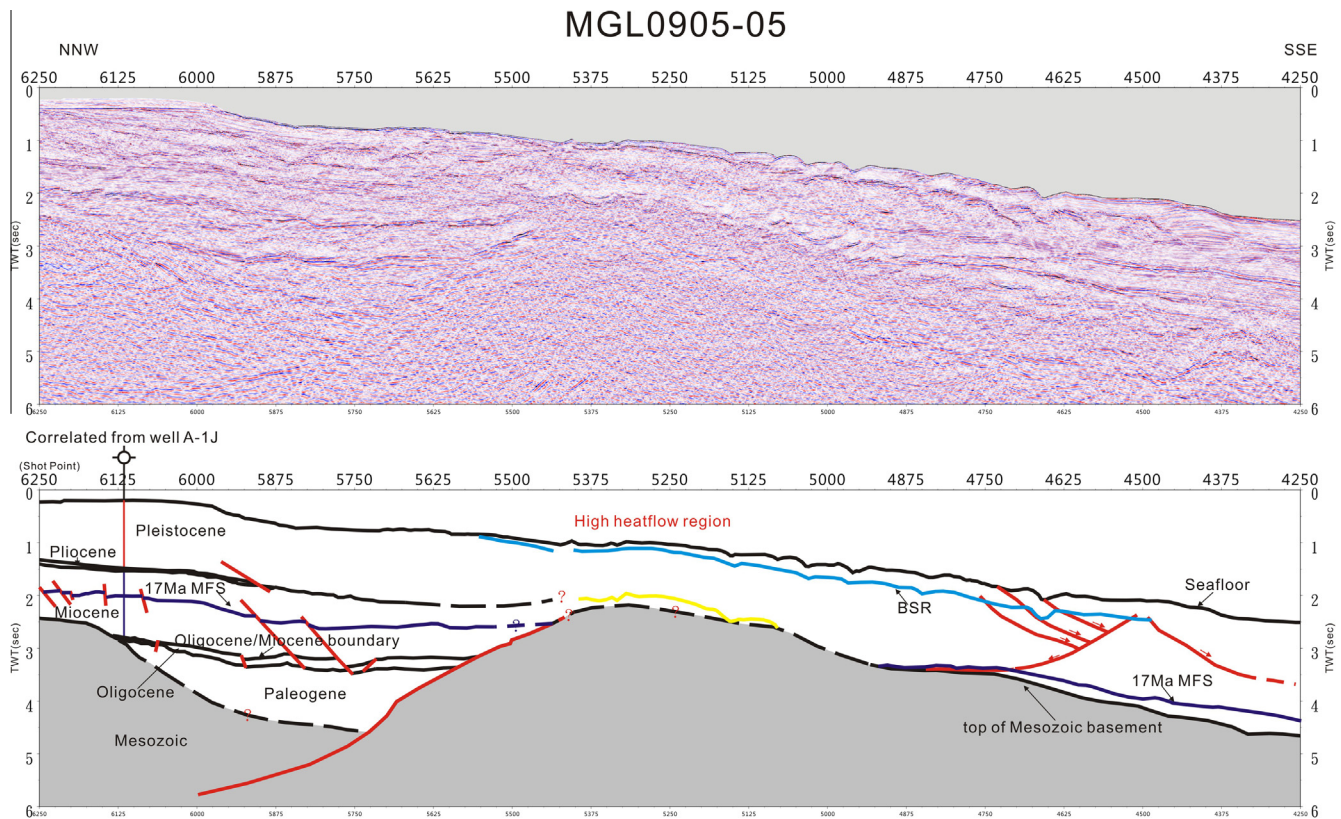


Fig. 10. Seismic section of MGL0905-05 running perpendicular to the continental slope and along the Jiulong Ridge in the west of the study area. The upper profile is uninterpreted and the interpreted profile is shown in the lower panel. Half graben and half graben-bounding fault are clearly seen in this profile. The stratigraphic ages are correlated from A-1J well located near the shelf edge. Profile location is shown in Figs. 2 and 8.

in relatively low geothermal gradients and heat flow observed at shallow depths in the continental shelf. The high geothermal gradients and heat flow in the slope region may be due to relatively thinner sedimentary cover (comparing to the Tainan Basin in the shelf region, Sibuet et al., 2002; Lin et al., 2003), highly extended crust (Lester et al., 2012) and extensive Cenozoic volcanic activity in the deeper water region (Sibuet et al., 2002; Wang et al., 2012; Yeh et al., 2012).

In the slope region, an area with anomalously high thermal gradients and heat flow is found in the northern part of the Jiulong Ridge at water depths ranging from 700 to 1000 m (Fig. 7b). BSR sub-bottom depth is shallower than 50 m at a water depth around 600 m. In such shallow water depths, BSRs are rarely found (Fig. 8). A half graben bounded by a north-dipping master fault, with more than 3.5 s two-way travel time [TWT] sediment infill, is discovered beneath northern Jiulong Ridge (Fig. 10). This half-graben bounding fault is a crust-penetrating fault (Lester et al., 2012). By correlating the stratigraphy from A-1J well, we are able to identify the basin infill of this half graben to be of Paleogene age and this half-graben is interpreted to have developed prior to seafloor spreading of the South China Sea in response to the rifting of the South China continent (Teng and Lin, 2004). The region of local high heat flow coincides with the footwall of this graben-bounding fault and local basement high (Fig. 10). Though this bounding fault has been inactive since the Miocene as evidenced by seismic sections shown, for example, in Fig. 10, part of this half graben-bounding fault and its Mesozoic basement at the footwall are exposed at the seafloor due to canyon erosion to the west of the Jiulong Ridge (Fig. 11).

The Cenozoic sediment cover thins toward the footwall of the Mesozoic basement near the bounding fault with sediment thickness only around 1–1.5 s TWT (Fig. 10). We speculated that

thinner sediments on top of the Mesozoic basement at the footwall may further result in higher heat flow observed in the Jiulong Ridge. In addition, this crust-penetrating half graben-bounding fault is likely to serve as an effective convection belt for hotter fluids at depths to reach to shallower depths. This will further enhance heat flows as observed near the fault zone in the Jiulong Ridge.

Though the slope region is characterized by high heat flow, the Formosa Ridge exhibits anomalously low geothermal gradients and heat flow (Fig. 7). The Formosa Ridge is a slope ridge of about 1 km in height and around 5 km in width. This ridge is characterized by anomalously deep BSR sub-bottom depth, reaching around 400 m beneath the ridge axis (Fig. 8). Chen et al. (2012) indicate that relatively deep BSR sub-bottom depths and low geothermal gradient are a result of sea water invading from the ridge flanks and seeping near the ridge top. Cold sea water invades and reduces the rock temperature moving the base of gas hydrate stability zone downward to a deeper depth beneath the Formosa Ridge.

We compare our results with the neighboring rifted margin to the west and the accretionary wedge to the east. Heat flow in the northern SCS margin mostly ranges in between 60 and 80 mW/m² (He et al., 2001 and Shi et al., 2003). To the west of our study area and in the Pearl River Mouth Basin, Yuan et al. (2009) pointed out that the geothermal gradient increases from the inner margin to the outer margin, from around 25–70 °C/km. The trend of increasing geothermal gradients toward the outer margin is consistent with our results obtained in the Tainan Basin, attesting that the BSR-derived thermal estimates are reliable.

To the east of the study area and in the submarine Taiwan accretionary wedge, the average heat flow is 43.4 ± 12.5 mW/m² (derived from BSRs, Chi and Reed, 2008) or 64 mW/m² (from heat probe measurements at the seafloor sediments, Shyu et al., 2006).

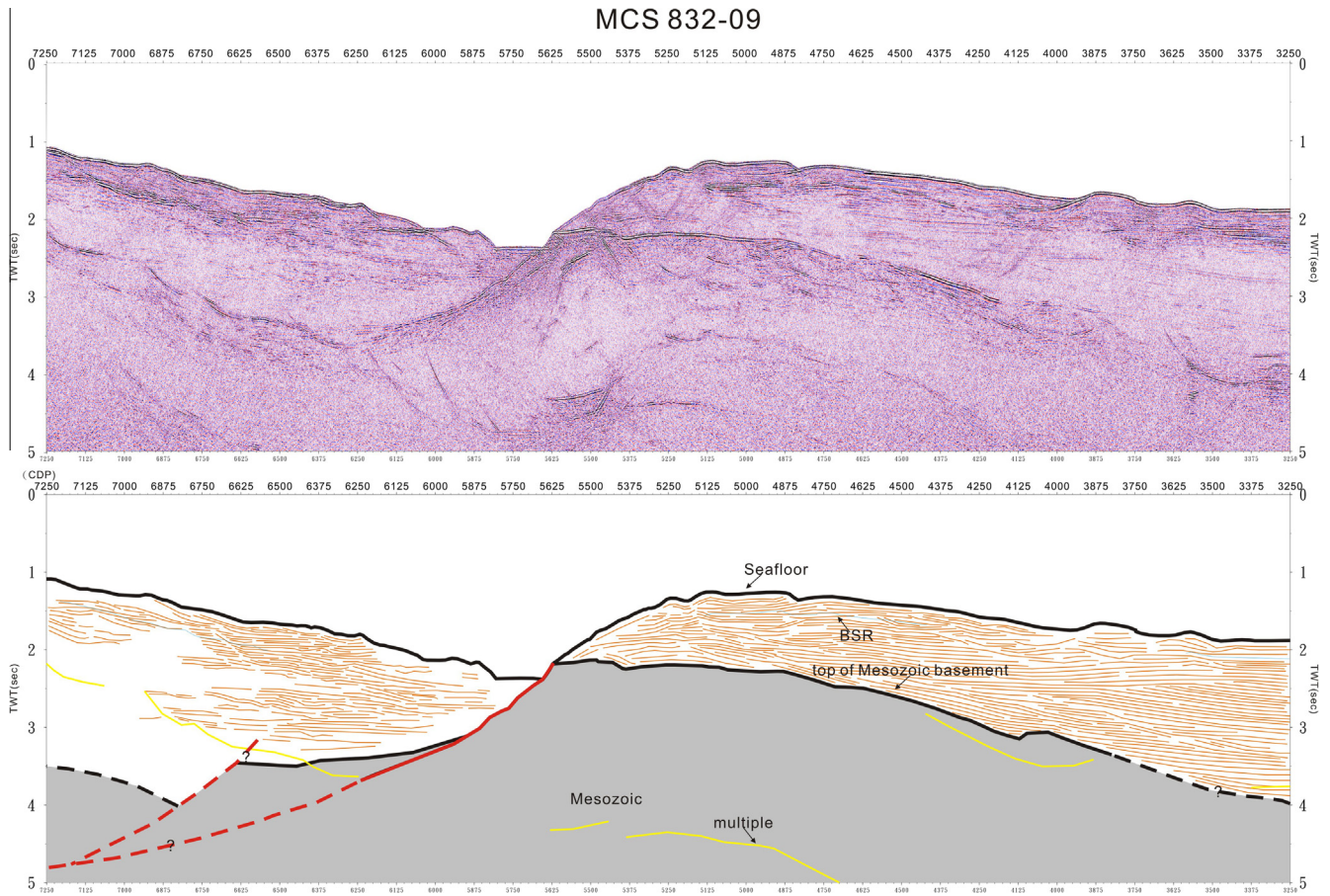


Fig. 11. Un-interpreted (upper panel) and interpreted (lower panel) seismic section of MCS832-09, running along the western flank of the Jiulong Ridge, showing the half graben-bounding fault (shown as red lines) and the Mesozoic basement at the footwall are exposed at the seafloor. See Figs. 2 and 8 for profile location. (For interpretation of the references to color in this figure legend, the reader is referred to the web version of this article.)

These values are slightly smaller than those obtained for the Tainan Basin.

We caution that there is an uncertainty for the derived geothermal gradients and heat flows. For hydrocarbon exploration wells, the uncertainty is mostly originated from obtaining true formation temperatures. Previous studies (e.g., Walpes and Ramly, 2001; Waples and Pedersen, 2004) argued that temperatures obtained from Horner-plot method are generally lower than “true” formation temperatures. Therefore the obtained temperatures should be considered as lower bounds.

In the slope region, the thermal regime is derived from BSRs seen from seismic sections. The uncertainty for calculating geothermal gradients and heat flows lies mostly in time-to-depth conversion for true BSR sub-bottom depths or factors controlling the base of gas hydrate stability zone (e.g., Minshull and White, 1989; Nillinger et al., 2010). As reported in Nillinger et al. (2010) the uncertainty for BSR-derived heat flux is difficult to assess if there is no drill data available for comparison.

6. Conclusions

Our study of geothermal gradients and heat flows in the rifted continental margin of the South China Sea offshore southwestern Taiwan shows that geothermal gradients in this region span in a range of 28–128 °C/km in the slope region, and 24–41 °C/km in shelf region; heat flows ranges in between 40 and 159 mW/m² in the slope region and 39–77 mW/m² in the shelf region. The geothermal gradients/heat flow increases from the inner margin to

the outer margin due mainly to thicker sediments in the inner margin and higher lithospheric thinning toward the outer margin. A local anomalously high heat-flow area is found to be associated with a half graben-bounding fault and its footwall in the slope region. This local heat-flow anomaly high indicates that the graben-bounding fault may serve as an efficient fluid conduit tapping hotter fluids from deeper crust.

Our study reveals that Tainan Basin is a little cooler than others in northern margin of South China Sea in the west and hotter than Taiwan accretionary wedge in the east. The major factor which affects geothermal gradient/heat flow in northern South China Sea margin is tectonic evolution of South China Sea, but some local anomalies are caused by sedimentation or local bathymetry effects beneath bathymetric ridges.

Acknowledgements

We thank Drs. Louis S. Teng, Che-Chuan Lin and Wu-Cheng Chi for discussion. Comments from two reviewers, Dr. Christian Berndt and the other anomalous one, greatly improve the quality of this paper. This study is funded by Central Geological Survey, Ministry of Economic Affairs and National Science Council.

References

- Allen, P.A., Allen, J.R., 2005. *Basin Analysis: Principles and Applications*, second ed. Blackwell Scientific Publications, Oxford.
- Beardsmore, G.R., Cull, J.P., 2001. *Crustal Heat Flow: A Guide to Measurement and Modelling*. Cambridge University Press.

- Briais, A., Patriat, P., Tapponnier, P., 1993. Updated interpretation of magnetic anomalies and seafloor spreading stages in the South China Sea: implications for the Tertiary Tectonics of Southeast Asia. *J. Geophys. Res.* 98 (B4), 6299–6328.
- Chi, W.-C., Reed, D., 2008. Evolution of shallow, crustal thermal structure from subduction to collision: an example from Taiwan. *GSA Bull.* 120 (5/6), 679–690.
- Chi, W.-C., Reed, D.L., Moore, G., Nguyen, T., Liu, C.-S., Lundberg, N., 2003. Tectonic wedging along the rear of the offshore Taiwan accretionary prism. *Tectonophysics* 374, 199–217.
- Chen, L., Wu, S.-K., Chi, W.-C., Liu, C.-S., 2012. Two Dimensional Fluid Flow Models Offshore Southwestern Taiwan. European Geosciences Union 2012. Vienna, Austria.
- Chiu, J.-K., Tseng, W.-H., Liu, C.-S., 2006. Distribution of gassy sediments and mud volcanoes offshore southwestern Taiwan. *Terr., Atmos. Ocean. Sci.* 17, 703–722.
- Clift, P., Lin, J., 2001. Preferential mantle lithospheric extension under the South China margin. *Mar. Pet. Geol.* 18, 929–945.
- Cloetingh, S., van Wees, J.D., Ziegler, P.A., Lenkey, L., Beekman, F., Tesauro, M., Forster, A., Norden, B., Kaban, M., Hardebol, N., Bonte, D., Genter, A., Guillou-Frottier, L., Ter Voorde, M., Sokoutis, d., Willingshofer, E., Cornu, T., Worum, G., 2010. Lithosphere tectonics and thermo-mechanical properties: an integrated modelling approach for enhanced geothermal systems exploration in Europe. *Earth Sci. Rev.* 102, 159–206.
- Gayet, P., dicharry, C., Marion, G., Graciaa, A., Lachaise, J., Vesterov, A., 2005. Experimental determination of methane hydrate dissociation curve up to 55 MPa by using a small amount of surfactant as hydrate promoter. *Chem. Eng. Sci.* 60, 5751–5758.
- Han, X., Suess, E., Huang, Y., Wu, N., Eisentauer, A., Bohrmann, G., Su, X., Abegg, F., Tao, J., Fan, Y., and shipboard scientists of Leg SO-177, 2005. Jiulong Methane Reef: First Direct Evidence of Methane Seepage in the South China Sea. European Geosciences Union 2005. Vienna, Austria.
- He, L., Wang, K., Xiong, L., Wang, J., 2001. Heat flow and thermal history of the South China Sea. *Phys. Earth Planet. Inter.* 126, 211–220.
- Horner, D.R., 1951. Pressure build-up in wells. *Proc. Third World Petrol. Congr., Hague 2*, 924–931.
- Houbolt, J.J.H.C., Wells, P.R.A., 1980. Estimation of heat flow in oil wells based on a relation between heat conductivity and sound velocity. *Geol. Mijnbouw* 59 (3), 215–224.
- Hyndman, R.D., Foucher, J.P., Yamano, M.Y., fishir, A., 1992. Deep sea bottom-simulating reflectors: calibration of the base of the hydrate stability field as used for heat flow estimates. *Earth Planet. Sci. Lett.* 109, 289–301.
- Lachenbruch, A.H., Brewer, M.C., 1959. Dissipation of the temperature effect of drilling a well in Arctic Alaska. *US Geol. Surv. Bull.* 1083-C, 73–109.
- Lee, T.-Y., Tang, C.-H., Ting, J.-S., Hsu, Y.-Y., 1993. Sequence stratigraphy of the Tainan Basin, offshore southwestern Taiwan. *Petrol. Geol. Taiwan* 28, 119–158.
- Lester, R., Lavier, L.L., McIntosh, K., Van Avendonk, H.J.A., Wu, F., 2012. Active extension in Taiwan's precollision zone: a new model of plate bending in continental crust. *Geology* 40, 831–834.
- Li, C.-F., Zhou, Z., Li, J., Hao, H., Geng, J., 2007. Structures of the northeasternmost South China Sea continental margin and ocean basin: geophysical constraints and tectonic implications. *Mar. Geophys. Res.* 28, 59–79.
- Li, L., Lei, X., Zhang, X., Sha, Z., 2013. Gas hydrate and associated free gas in the Dongsha Area of northern South China Sea. *Mar. Pet. Geol.* 39, 92–101.
- Lin, A.T., Watts, A.B., 2002. Origin of the West Taiwan Basin by orogenic loading and flexure of a rifted continental margin. *J. Geophys. Res.* 107 (B9), 2185. <http://dx.doi.org/10.1029/2001JB000669>.
- Lin, A.T., Watts, A.B., Hesselbo, S.P., 2003. Cenozoic stratigraphy and subsidence history of the South China Sea margin in the Taiwan region. *Basin Res.* 15, 453–478.
- Lin, A.T., Liu, C.-S., Lin, C.-C., Schnurle, P., Chen, G.-Y., Liao, W.-Z., Teng, L.S., Chuang, H.-J., Wu, M.-S., 2008. Tectonic features associated with the overriding of an accretionary wedge on top of a rifted continental margin: an example from Taiwan. *Mar. Geol.* 255, 186–203.
- Lin, C.-C., Lin, A.T., Liu, C.-S., Chen, G.-Y., Liao, W.-Z., Schnurle, P., 2009. Geological controls on BSR occurrences in the incipient arc-continent collision zone off southwest Taiwan. *Mar. Pet. Geol.* 26, 1118–1131.
- Lin, C.-C., Lin, A.T., Liu, C.-S., Hornig, C.-S., Chen, G.-Y., Wang, Y., 2013. Canyon-infilling and gas hydrate occurrences in the frontal fold of the offshore accretionary wedge off southern Taiwan. *Mar. Geophys. Res.* <http://dx.doi.org/10.1007/s11001-013-9203-7>.
- Liu, C.-S., Liu, S.-Y., Lallemand, S., Lundberg, N., Reed, D.L., 1998. Digital elevation model offshore Taiwan and its tectonic implication. *Terr., Atmos. Ocean. Sci.* 9, 705–738.
- Liu, C.-S., Deffontaines, B., Lu, C.-Y., Lallemand, S., 2004. Deformation patterns of an accretionary wedge in the transition zone from subduction to collision offshore southwestern Taiwan. *Mar. Geophys. Res.* 25, 123–137.
- Liu, C.-S., Schnurle, P., Wang, Y., Chung, S.-H., Chen, S.-C., Hsuan, T.-H., 2006. Distribution and characters of gas hydrate offshore of southwestern Taiwan. *Terr., Atmos. Ocean. Sci.* 17, 615–644.
- Minshull, T.A., White, R., 1989. Sediment compaction and fluid migration in the Makran accretionary prism. *J. Geophys. Res.* 94 (6), 7387–7402.
- Nillinger, H., Trehu, A.M., Grevenmeyer, I., 2010. Seafloor Marine Heat Flux Measurements and Estimation of Heat Flux from Seismic Observations of Bottom Simulating Reflectors. Geophysical Characterization of Gas Hydrates, Special volume, 279–298, ISBN (13) 9181560802181, Society of Exploration Geophysicists.
- Shi, X., Qiu, X., Xia, K., Zhou, D., 2003. Characteristics of surface heat flow in the South China Sea. *J. Asian Earth Sci.* 22, 265–277.
- Shyu, C.-T., Chen, Y.-J., Chiang, S.-T., Liu, C.-S., 2006. Heat flow measurement over bottom simulating reflectors, offshore southwestern Taiwan. *Terr., Atmos. Ocean. Sci.* 17 (4), 845–869.
- Sibuet, J.C., Hsu, S.-K., Le Pichon, X., Le Formal, J.P., Reed, D., Moore, G., Liu, C.-S., 2002. East Asia plate tectonics since 15 Ma: constraints from the Taiwan region. *Tectonophysics* 344, 103–134.
- Stoll, R.D., Ewing, J., Bryan, G.M., 1971. Anomalous velocities in sediments containing gas hydrate. *J. Geophys. Res.* 76, 2090–2094.
- Suess, E., 2005. RV SONNE Cruise Report SO 177, Sino-German Cooperative Project, South China Sea Continental Margin: Geological Methane Budget and Environmental Effects of Methane Emissions and Gas Hydrate. IFM-GEOMAR Reports. <http://store.pangaea.de/documentation/Reports/SO177.pdf> (assessed 28.11.13).
- Tang, F.-S., Oung, J.-N., Hsu, Y.-Y., Yang, C.-N., 1999. Elementary study of structural evolution in Tainan Basin in southwest Taiwan Strait. *Petrol. Geol. Taiwan* 33, 125–149 (in Chinese).
- Taylor, B., Hayes, D.E., 1983. Origin and history of the South China Sea Basin. In: Hayes, C.E. (Ed.), *The Tectonic and Geologic Evolution of Southeast Asian Seas and Islands 2*. American Geophysical Union, Geophysical Monograph, vol. 27, pp. 23–56.
- Teng, L.S., Lin, A.T., 2004. Cenozoic tectonics of the China continental margin: Insights from Taiwan. In: Malpas, J., Fletcher, C.J., Aitchinson, J.C., Ali, J. (Eds.), *Aspects of the Tectonic Evolution of China*, Special Publications ed., 226. Geological Society, London, pp. 313–332.
- Tsao, W.C.Q., Oung, J.-N., Yang, C.-M., Lee, Y.-W., Wang, M.-H., Uang, Y.-C., Tang, S.-L., 1992. Studies on hydrocarbon potential of Mesozoic formation in the Tainan Basin, southwestern offshore Taiwan. *Min. Metall.* 36 (1), 32–45 (in Chinese).
- Tzeng, J., Uang, Y.-C., Hsu, Y.-Y., Teng, L.S., 1996. Seismic stratigraphy of the Tainan Basin. *Petrol. Geol. Taiwan* 30, 281–308 (in Chinese).
- Wang, K.-L., Lo, Y.-M., Chung, S.-L., Lo, C.-H., Hsu, S.-K., Yang, H.-J., Shinjo, R., 2012. Age and geochemical features of dredged basalts from offshore SW Taiwan: the coincidence of intra-plate magmatism with the spreading South China Sea. *Terr., Atmos. Ocean. Sci.* 23 (6), 657–669.
- Watson, M.P., Hayward, A.B., Parkinson, D.N., Zhang, Z.M., 1987. Plate tectonic history, basin development and petroleum source rock deposition in onshore China. *Mar. Petrol. Geol.* 4, 205–225.
- Waples, D.W., Pedersen, M.R., 2004. Evaluation of Horner plot-corrected log-derived temperatures in the Danish Central Graben, North Sea. *Nat. Resour. Res.* 13 (4), 223–227.
- Walpes, D.W., Ramly, M., 2001. A statistical method for correcting log-derived temperatures. *Petrol. Geosci.* 7 (3), 231–240.
- Wu, J.-M., 1988. Cenozoic basins of the South China Sea. *Episodes* 11, 91–96.
- Yamano, M., Foucher, J.P., Kinoshita, M., Fisher, A., Hyndman, R.D., ODP Leg 131 Shipboard Scientific Party, 1992. Heat flow and fluid flow regime in the western Nankai accretionary prism. *Earth Planet. Sci. Lett.* 109, 451–462.
- Yang, K.-M., Ting, H.-H., Yuan, J., 1991. Structural styles and tectonic models of Neogene extensional tectonics in southwestern Taiwan: implications for hydrocarbon exploration. *Petrol. Geol. Taiwan* 26, 1–31.
- Yeh, Y.-C., Hsu, S.-K., Doo, W.-B., Sibuet, J.C., Liu, C.-S., Lee, C.-S., 2012. Crustal features of the northeastern South China Sea: insights from seismic and magnetic interpretations. *Mar. Geophys. Res.* 1–20.
- Yu, H.-S., 1990. The Pearl River Mouth Basin: a rift basin and its geodynamic relationship with the southeastern Eurasian margin. In: J. Angelier (Ed.), *Geodynamic Evolution of the Eastern Eurasian Margin*. Tectonophysics, vol. 183, pp. 177–186.
- Yu, H.-S., 1994. Structure, stratigraphy and basin subsidence of Tertiary basins along the Chinese southeastern continental margin. *Tectonophysics* 235, 63–76.
- Yu, H.-S., Hong, -E., 2006. Shifting submarine canyons and development of a foreland basin in SW Taiwan: controls of foreland sedimentation and longitudinal sediment transport. *J. Asian Earth Sci.* 27, 922–932.
- Yuan, Y., Zhu, W., Mi, L., Zhang, G., Hu, S., He, L., 2009. "Uniform geothermal gradient" and heat flow in the Qiongdongan and Pearl River Mouth Basins of the South China Sea. *Mar. Pet. Geol.* 26, 1152–1162.